RSC Advances

PAPER

View Article Online
View Journal | View Issue



Cite this: *RSC Adv.*, 2019, **9**, 20439

# Efficient detoxification of triclosan by a S–Ag/$TiO_2$@g-$C_3N_4$ hybrid photocatalyst: process optimization and bio-toxicity assessment †

Xiangfeng Xie,[ab] Chen Chen,[a] Xiaoxiang Wang,[ac] Jie Li*[ac] and Saraschandra Naraginti *[cd]

Received 2nd May 2019
Accepted 24th June 2019

DOI: 10.1039/c9ra03279g

rsc.li/rsc-advances

Owing to their persistency and toxicity, development of an effective strategy to eliminate antibiotic residues from the aquatic system has become a major environmental concern. Doping $TiO_2$ with hetero atoms and forming a hybrid structure with g-$C_3N_4$ could serve as an efficient visible light active photocatalytic candidate. In this study, a novel S–Ag/$TiO_2$@g-$C_3N_4$ hybrid catalyst was prepared for visible light degradation and detoxification of triclosan (TS) antibiotic. The effect of various operational parameters towards the photocatalytic degradation was systematically evaluated through response surface methodology (RSM) based on central composite design (CCD). The highest TS degradation (92.3%) was observed under optimal conditions (TS concentration = 10 mg $L^{-1}$, pH = 7.8, and catalyst weight = 0.20 g $L^{-1}$) after 60 min. Efficient charge separation resulted from the doped nanoparticles (silver and sulphur), the existing integrated electric field of the heterojunction and the overlying light response of hybridized $TiO_2$ and g-$C_3N_4$, thus the S–Ag/$TiO_2$@g-$C_3N_4$ composite showed impressively higher activity. The main degradation products of TS were identified by LC/ESI-MS analysis. In addition, the toxicity of the degradation products was investigated through an *Escherichia coli* (*E. coli*) colony forming unit assay and the results revealed that under optimal conditions a significant reduction in biotoxicity was noticed.



## 1. Introduction

The continuous and long-term usage of antibiotics has raised important environmental concerns since these antibiotics are being detected in lakes, rivers and wastewater effluents and is thought to be the reason for the increment in antibiotic resistant bacteria and genes.[1,2] For instance, during 2013 China consumed about 92 700 tons of antibiotics in which 53 800 tons were released into the environment.[3] Triclosan is a bactericidal agent which has been added to many PCPs (personal care products) like soap, toothpaste, shampoo *etc.*[4] However, triclosan has been detected in wastewater and confirmed to be dangerous to many organisms and humans.[5] This necessitates the removal or decomposing of triclosan from the environment to safe guard human beings[6] and other organisms. However, as a recalcitrant pollutant triclosan is difficult to eliminate by conventional wastewater treatment methods. Moreover, physicochemical and biological technologies do not exhibit an excellent outcome to deal with triclosan.[7] This necessitates the development of efficient materials and tertiary oxidative treatments for the enhanced degradation of triclosan.

Advanced Oxidation Processes (AOPs) are conceived as one of the most attracting solutions because of their rapidity and non-selective degradation power towards a wide range of organic compounds.[8] $TiO_2$ is one of the best photocatalytic materials due its stability, non-toxicity, low cost and high performance,[9] but its band gap (~3.2 eV) and higher recombination rate restricting its usage in practical applications.[10] Doping $TiO_2$ matrix with metal and non-metal dopants has attracted significant attention since they can exhibit higher photo-catalytic activity and unique characteristics.[11–14] Even so, the dopants should be in small quantities to suppress the recombination of photo-generated electrons and holes.[15] Hence, the low concentration doping could be an effective solution to enhance the visible light absorption efficiency.

Recently, graphitic carbon nitride (g-$C_3N_4$) has pulled ample scientific interests because of its suitable band gap, stability and efficient transferability to further enhance the light harvesting capacity of $TiO_2$ based photocatalysts.[16,17] Though g-$C_3N_4$ is visible light active material, its UV response is relatively lower, when compared to $TiO_2$.[18] Coupling lower bandgap g-$C_3N_4$ with higher bandgap $TiO_2$ doped with metal and non-metal atoms as visible

[a]*Jiangsu Academy of Environmental Industry and Technology Corp., Nanjing 210036, China. E-mail: enveng@126.com*

[b]*School of Energy and Environment, Key Laboratory of Environmental Medicine Engineering of the Ministry of Education, Southeast University, Nanjing 210096, China*

[c]*Ministry of Education Key Laboratory of Integrated Regulation and Resource Development on Shallow Lakes, College of Environment, Hohai University, Nanjing 210098, China*

[d]*Biofuels Institute, School of the Environment, Jiangsu University, 301 Xuefu Road, Zhenjiang 212013, China. E-mail: saras@ujs.edu.cn*

† Electronic supplementary information (ESI) available. See DOI: 10.1039/c9ra03279g

light sensitizer to form a heterojunction can superimpose the light response activity of both the semiconductors, owing to the special electronic band structure.[19,20] Furthermore, heterojunction formation is a promising scheme to improve charge separation, by the build-in electric field of heterojunction which can drive the photogenerated electrons and holes to transfer to opposite directions, therefore inhibiting their recombination.[21] Thus, it is suitable to harvest more sunlight through the combination of g-$C_3N_4$ and $TiO_2$ forming the g-$C_3N_4$/$TiO_2$ heterojunction.

The optimization of operational parameters is an important strategy to improve photocatalytic efficiency to obtain satisfactory degradation of organic pollutants. Response surface methodology (RSM) is a statistical and experimental strategy to get the optimum conditions for a multivariable system and it has been successfully applied to a different photocatalytic processes for achieving its optimization using experimental designs.[22–24]

This study aims to fabricate Ag and S co-doped $TiO_2$@g-$C_3N_4$ hybrid photocatalyst for efficient degradation of triclosan antibiotic. The plausible mechanism of degradation for the efficient catalytic activity of the S–Ag/$TiO_2$@g-$C_3N_4$ hybrid composite was proposed. Furthermore, response surface methodology was successfully applied for optimizing and maximizing the degradation. In addition, water reuse demands the toxicity assessment of triclosan and its degradation products. Hence the biotoxicity of triclosan and its degradation products was also investigated on *E. coli* to define the environmental impact of the treated water.

# 2. Experimental

## 2.1 Materials

Titanium(IV) isopropoxide (95%), silver nitrate (≥99.8%), thiourea (≥99.5%), 2-propanol (≥99.5%), Tween 20 (≥99%), hydrazine hydrate (≥80%), melamine (99%) and triclosan (97%) were obtained with analytical grade from Alibaba chemicals and used without further purification.

## 2.2 Preparation of the photocatalyst

First, the g-$C_3N_4$ was synthesized according to previous report.[25] In brief, 5 g of melamine was heated at 600 °C for 2 h at a heating rate of 2 °C $min^{-1}$ in a muffle furnace; the obtained faint yellow colored g-$C_3N_4$ was naturally cooled to room temperature. Later, a calculate amount of g-$C_3N_4$ (0.1 g) and 5 mL of titanium isopropoxide (TTIP) was dispersed in 50 mL of isopropanol which was further added to 200 mL of distilled water at pH ~ 1.5. To the above solution required amounts of $AgNO_3$ and thiourea aqueous solutions were added followed by 5 mL of Tween 20 while stirring. The resultant sol was then sonicated at 80 MHz for 90 min. The obtained gel was further dried followed by calcination at 400 °C for 5 h and denoted as S/Ag–$TiO_2$@g-$C_3N_4$. Ag–$TiO_2$@g-$C_3N_4$ nanoparticles were also prepared as described in the above method without addition of thiourea. For control experiment, $TiO_2$ nanoparticles were prepared as follows; a mixture of 5 mL of titanium(IV) isopropoxide in 50 mL isopropanol was added dropwise to 200 mL of distilled water maintained at pH 1.5 while the solution was continuously stirred. This $TiO_2$ sol was dried at 100 °C for 24 h, followed by calcination at 400 °C for 5 h.

## 2.3 Characterization techniques

BRUKER D8 Advance X-ray diffractometer was used for XRD analysis with Cu $K_\alpha$ source ($\lambda$ = 1.5406 Å). For imaging a high resolution transmission electron microscope was used (TEM, FEI TecnaiG2 F20 S-TWIX, at 200 KV) at different magnifications. JASCO V-670 UV-Vis spectrophotometer was used for diffused reflectance spectra analysis. Raman analysis was carried out by using Thermo Scientific DXR2 at room temperature. XPS data was acquired using Kratos Axis Ultra 165 spectrometer with a monochromated Al K$\alpha$ X-ray source ($h\alpha$ = 1486.6 eV).

## 2.4 Photocatalytic degradation of triclosan

A 250 W Xe lamp was used as the visible light source with a filter ($\lambda \leq$ 420 nm). The samples at regular intervals were collected and the concentration of leftover TS was analyzed using Agilent 1260 series HPLC equipped with Eclipse XDBC18 (5 μm) reverse phase column (4.6 × 150 mm). Water and acetonitrile at 30 : 70 v/v ratio was used as the mobile phase at an injection volume of 1 mL $min^{-1}$ for 10 minutes. Further, the degradation products identification was carried out by liquid chromatography tandem mass spectrometry (Agilent 1290 Infinity Binary LC system, Agilent 6460 Triple Quadrupole LCMS/MS system employing the Zorbax eclipse plus C18 column; rapid resolution, 2.1 × 50 mm, 1.8 μm). The mobile phase of water and acetonitrile at 30 : 70 (v/v) was used for about 60 min. To electro spray ionization (ESI) was used to obtain the mass spectra under the helium gas flow at approximately 1 mL $min^{-1}$ and 16 V of fragment voltage.

## 2.5 Experimental design

In the present study to optimize the degradation efficiency of TS, statistical modeling software Design-Expert®11 was utilized. Four independent variables *i.e.*, TS concentration, pH, photocatalyst weight and time were selected on the percentage degradation of TS as the response (dependent variable). The ranges and the levels of the independent variables are shown in Table 1. A Central Composite Design (CCD) based on RSM was employed for the evaluation of four operational factors effects on the photocatalytic degradation process. Table 2 represents the ranges of the factors along with the twenty four tests (24 runs) designed. Accordingly, the test results were fitted to a quadratic polynomial model intended by the software to correlate the measured responses with the independent factors (Table 2).

## 2.6 Biotoxicity assessment on *Escherichia coli*

The bio-toxicity assessment was determined by evaluating the growth of *E. coli* K-12 (CGMCC1.365) while treating with pure TS, degradation products and control (without TS). The solution's biotoxicity is reciprocal to the number of *E. coli* colonies grown on LB agar plates. In other words, the detoxification efficiency of the sample was inversely proportional to the growth inhibition of *E. coli* with respect to the control. The detoxification efficiency was calculated as follows:

 

Table 1 Experimental range and levels of the independent test variables

| | | Coded levels | | |
|---|---|---|---|---|
| Symbol | Variables | −1 | 0 | +1 |
| $X_1$ | TS concentration (mg $L^{-1}$) | 10 | 20 | 30 |
| $X_2$ | pH | 5 | 8 | 11 |
| $X_3$ | Catalyst weight (g $L^{-1}$) | 0.1 | 0.2 | 0.3 |
| $X_4$ | Time | 30 | 60 | 90 |

Table 2 Response surface central composite design (CCD) and their experimental results

| | Actual values | | | | Coded values | | | | Response | |
|---|---|---|---|---|---|---|---|---|---|---|
| Run | $X_1$ | $X_2$ | $X_3$ | $X_4$ | $X_1$ | $X_2$ | $X_3$ | $X_4$ | Actual | Predicted |
| 1 | 20 | 8 | 0.2 | 30 | 0 | 0 | 0 | −1 | 85.60 | 87.93 |
| 2 | 10 | 11 | 0.1 | 30 | −1 | +1 | −1 | −1 | 66.30 | 63.90 |
| 3 | 10 | 5 | 0.3 | 90 | −1 | −1 | +1 | +1 | 67.90 | 69.46 |
| 4 | 20 | 8 | 0.3 | 60 | 0 | 0 | +1 | 0 | 88.70 | 86.90 |
| 5 | 20 | 11 | 0.2 | 60 | 0 | +1 | 0 | 0 | 65.30 | 67.12 |
| 6 | 30 | 5 | 0.1 | 90 | +1 | −1 | −1 | +1 | 66.20 | 64.70 |
| 7 | 30 | 11 | 0.1 | 30 | +1 | +1 | −1 | −1 | 63.40 | 61.86 |
| 8 | 30 | 11 | 0.3 | 30 | +1 | +1 | +1 | −1 | 60.30 | 60.64 |
| 9 | 10 | 5 | 0.1 | 90 | −1 | −1 | −1 | +1 | 66.80 | 66.44 |
| 10 | 30 | 11 | 0.1 | 90 | +1 | +1 | −1 | +1 | 59.80 | 60.72 |
| 11 | 10 | 11 | 0.3 | 30 | −1 | +1 | +1 | −1 | 60.40 | 61.92 |
| 12 | 10 | 8 | 0.2 | 60 | −1 | 0 | 0 | 0 | 92.80 | 92.26 |
| 13 | 10 | 11 | 0.3 | 90 | −1 | +1 | +1 | +1 | 62.90 | 61.93 |
| 14 | 10 | 5 | 0.3 | 30 | −1 | −1 | +1 | −1 | 68.20 | 67.25 |
| 15 | 30 | 5 | 0.3 | 30 | +1 | −1 | +1 | −1 | 65.90 | 64.72 |
| 16 | 30 | 5 | 0.3 | 90 | +1 | −1 | +1 | +1 | 66.10 | 68.48 |
| 17 | 10 | 5 | 0.1 | 30 | −1 | −1 | −1 | −1 | 66.00 | 66.93 |
| 18 | 20 | 8 | 0.1 | 60 | 0 | 0 | −1 | 0 | 84.20 | 86.00 |
| 19 | 20 | 5 | 0.2 | 60 | 0 | −1 | 0 | 0 | 73.60 | 71.78 |
| 20 | 30 | 5 | 0.1 | 30 | +1 | −1 | −1 | −1 | 62.70 | 63.64 |
| 21 | 10 | 11 | 0.1 | 90 | −1 | +1 | −1 | +1 | 60.00 | 61.21 |
| 22 | 20 | 8 | 0.2 | 90 | 0 | 0 | 0 | +1 | 90.80 | 88.47 |
| 23 | 30 | 8 | 0.2 | 60 | +1 | 0 | 0 | 0 | 90.20 | 90.74 |
| 24 | 30 | 11 | 0.3 | 90 | +1 | +1 | +1 | +1 | 63.10 | 62.20 |

Inhibition rate of *E. coli* in the presence of TS ($X$)
= (no. of *E. coli* colonies in control)
− (no. of *E. coli* colonies in pure TS)

Inhibition rate of *E. coli* in the presence of degradation products ($Y$) = (no. of *E. coli* colonies in control)
− (no. of *E. coli* colonies in degradation products)

$$\text{Detoxification efficiency } (\%) = \left[\frac{X - Y}{X}\right] \times 100$$

# 3. Results and discussion

## 3.1 Characterization of nanocomposite

Fig. 1a represented the XRD patterns of the prepared pure $TiO_2$, g-$C_3N_4$, Ag/$TiO_2$@g-$C_3N_4$, and S–Ag/$TiO_2$@g-$C_3N_4$ photocatalysts. XRD pattern of pure g-$C_3N_4$ showed two distinct peaks at 13.3° and 27.3° which could be ascribed to (100) and (002) planes respectively (JCPDS: 87-1526).[26] The XRD pattern of Ag/$TiO_2$@g-$C_3N_4$ and S–Ag/$TiO_2$@g-$C_3N_4$ showed characteristic peaks for anatase phase with 2$\theta$ values at 25.3°, 37.7°, 47.7°, 55.0° and 62.5° which could be assigned to (101), (103), (004), (200), (105), (211), and (204) planes respectively (JCPDS: 21-1272). Due to lower dopant concentration, signals corresponded to Ag were not observed, this could be suggested that the doped metal atoms did not alter phase crystallinity of $TiO_2$.[27] The absence of g-$C_3N_4$ peaks in Ag/$TiO_2$@g-$C_3N_4$ and S/Ag–$TiO_2$@g-$C_3N_4$ was attributed to the combination of smaller and highly dispersed g-$C_3N_4$ particles with the other nanoparticles, or the hybridization had no significant effect on the crystal phase of $TiO_2$, in which the $TiO_2$ peaks were highly strong so as to hinder the g-$C_3N_4$ diffraction peaks.[19] Furthermore, Raman analysis was carried out to confirm the crystalline formation of the prepared $TiO_2$/g-$C_3N_4$ composites. As shown in Fig. 1b the pure $TiO_2$ showed peaks at 145, 395, 514 and 639 $cm^{-1}$ attributed to anatase $TiO_2$.[28] While all other composites showed additional two peaks at 1306 and 1589 $cm^{-1}$ which are attribute to $A_{1g}$ phonon pattern and $E_{2g}$ symmetric phonon vibration of the $k$ point in the graphite-like structure and disordered $sp^2$ micro-domains enclosed by linking with N atoms, showing the successful coupling of $TiO_2$ on the g-$C_3N_4$ sheet and the results are in complete agreement with the literature.[29,30] The inset of Fig. 1b shows the Raman spectrum of pure g-$C_3N_4$ with D and G bands located at 1306 and 1589 $cm^{-1}$ respectively.

The optical properties of the photocatalyst play a crucial role in deciding its catalytic activity, hence the UV-Vis absorption spectra of pure $TiO_2$, g-$C_3N_4$, Ag/$TiO_2$@g-$C_3N_4$ and S/Ag–$TiO_2$@g-$C_3N_4$ were investigated (Fig. S1a†). Pure $TiO_2$ did not show any absorption in the visible region because of its intrinsic wide band gap. However, the doped Ag could strongly absorb visible light due to its SPR effect.[31,32] $TiO_2$ nanoparticles doped with single atom (silver) showed lower shift in comparison to two atoms (sulphur and silver) (Fig. S1a†). g-$C_3N_4$ can absorb the light in UV and visible region up to 450 nm. However, g-$C_3N_4$ light adsorption potential in UV region is lower than $TiO_2$, in particular at lower light wavelengths (<300 nm). By coupling Ag/$TiO_2$ and S/Ag–$TiO_2$ with g-$C_3N_4$ it showed much higher absorption intensity than pure g-$C_3N_4$ and $TiO_2$ both in the UV and visible regions. Furthermore, the absorption edge of S/Ag–$TiO_2$@g-$C_3N_4$ had an evident higher red-shift when compare to g-$C_3N_4$ and Ag–$TiO_2$@g-$C_3N_4$ (Fig. S1b†). It is suggested that $TiO_2$ modified with sulphur and silver followed by coupling with g-$C_3N_4$ showed decrease in the band energy, revealed that the combination of g-$C_3N_4$ and S/Ag–$TiO_2$ not only led to an efficient light adsorption performance but also a narrowed band gap.

The TEM image shown in Fig. 2a indicated that the S/Ag doped $TiO_2$ nanoparticles were in agglomerated form with small irregular shape. The presence of Ag, $TiO_2$ and g-$C_3N_4$ was also observed in the TEM images. The high resolution TEM (HRTEM) image (Fig. 2b) evidently showed the close interface between the 2D flakes of g-$C_3N_4$ and S/Ag doped $TiO_2$ nanoparticles. The observed lattice spacing value of 0.33 nm was

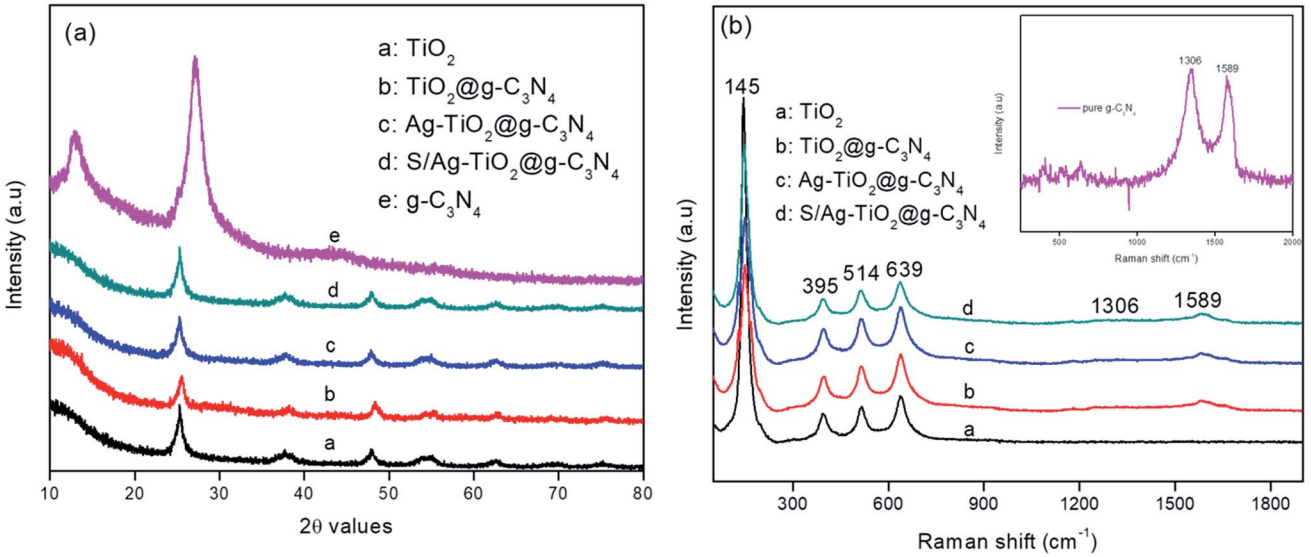


Fig. 1 (a) XRD patterns and (b) Raman spectra of the prepared composites; inset of (b) Raman spectra of pure g-$C_3N_4$.

ascribed to the (101) plane of anatase phase $TiO_2$ (JPCDS no. 78-2486), and the value of 0.21 nm was assigned to the (111) plane of cubic structure silver (JPCDS no. 89-3722). The close interfacial contact between doped $TiO_2$ and g-$C_3N_4$ is of extreme implication for alleviating the photo generated electrons to transfer from g-$C_3N_4$ to S/Ag doped $TiO_2$.[33]

XPS analysis was carried out for S/Ag–$TiO_2$@g-$C_3N_4$ in order to investigate the elemental composition of the prepared catalyst. Fig. 3a showed the survey spectrum which indicated the presence of C, N, Ti, O, Ag, and S elements in the prepared catalyst. The high-resolution XPS spectrum of Ag at 3d core levels (Fig. 3b) revealed that the Ag $3d_{5/2}$ and Ag $3d_{3/2}$ binding energies were observed at 368.3 and 374.2 eV respectively indicates the presence of $Ag^0$.[34,35] The S 2p spectra (Fig. 3c) showed two peaks at 169.8 eV and 170.2 eV, which could be ascribed to S $2p_{3/2}$ and S $2p_{1/2}$, respectively. This could be emphasized that the S cations in the sample are present in $S^{6+}$ state which is similar to the previous studies.[36,37] The Ti $2p_{3/2}$ and Ti $2p_{1/2}$ binding energies (Fig. 3d) were observed at 459.3 and 464.7 eV respectively.[38,39] Fig. 3e represents the C 1s spectra, in which the peak at 284.7 eV was attributed to the surface unessential carbon or $sp^2$ C–C bonds. The peaks at 286.4 eV and 288.1 eV attributed to C–O and C–N–C groups of g-$C_3N_4$, respectively.[33,40] Fig. 3f showed the high resolution XPS spectrum of N, in which peaks at 398.7, 399.6, and 401.2 eV were corresponded to $sp^2$ hybridized aromatic N bonded to carbon atoms (C=N–C), the tertiary N bonded to carbon atoms in the form of N–$(C)_3$, and N–H side groups, respectively.[40] The week peak at 404.6 eV was ascribed to the π-excitations.[33,41] From the XPS results the atomic percentages of Ag, S, Ti, C, O and N elements in S/Ag–$TiO_2$@g-$C_3N_4$ composite were found to be 5.75, 2.16, 16.04, 29.29, 34.91 and 11.85 respectively.

### 3.2 Modeling, optimization and kinetics

The photocatalytic degradation of triclosan by S/Ag–$TiO_2$@g-$C_3N_4$ nanocomposite was modeled through RSM framework by

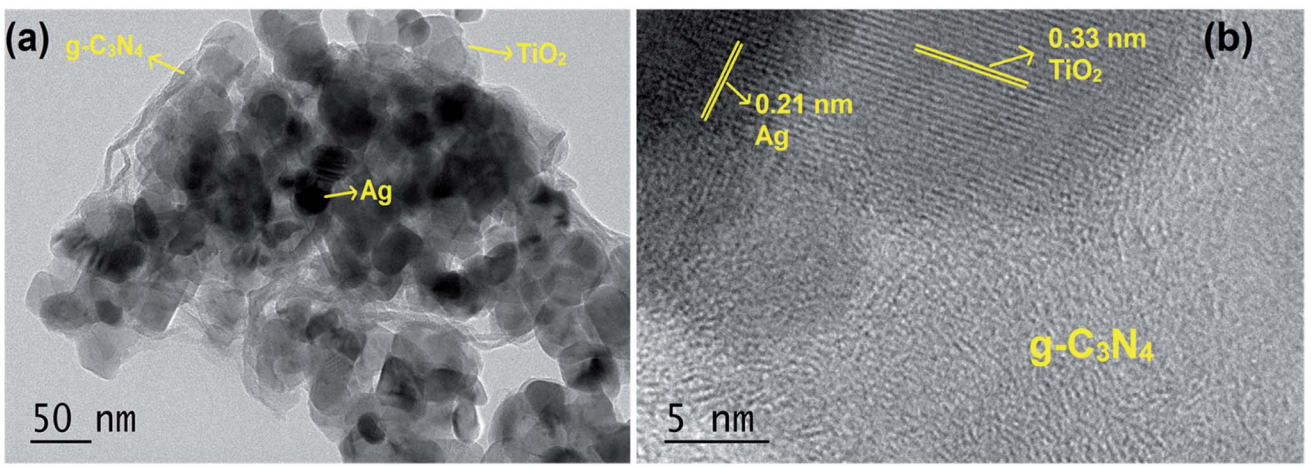


Fig. 2 (a) TEM image and (b) HRTEM image of S/Ag–$TiO_2$@g-$C_3N_4$.

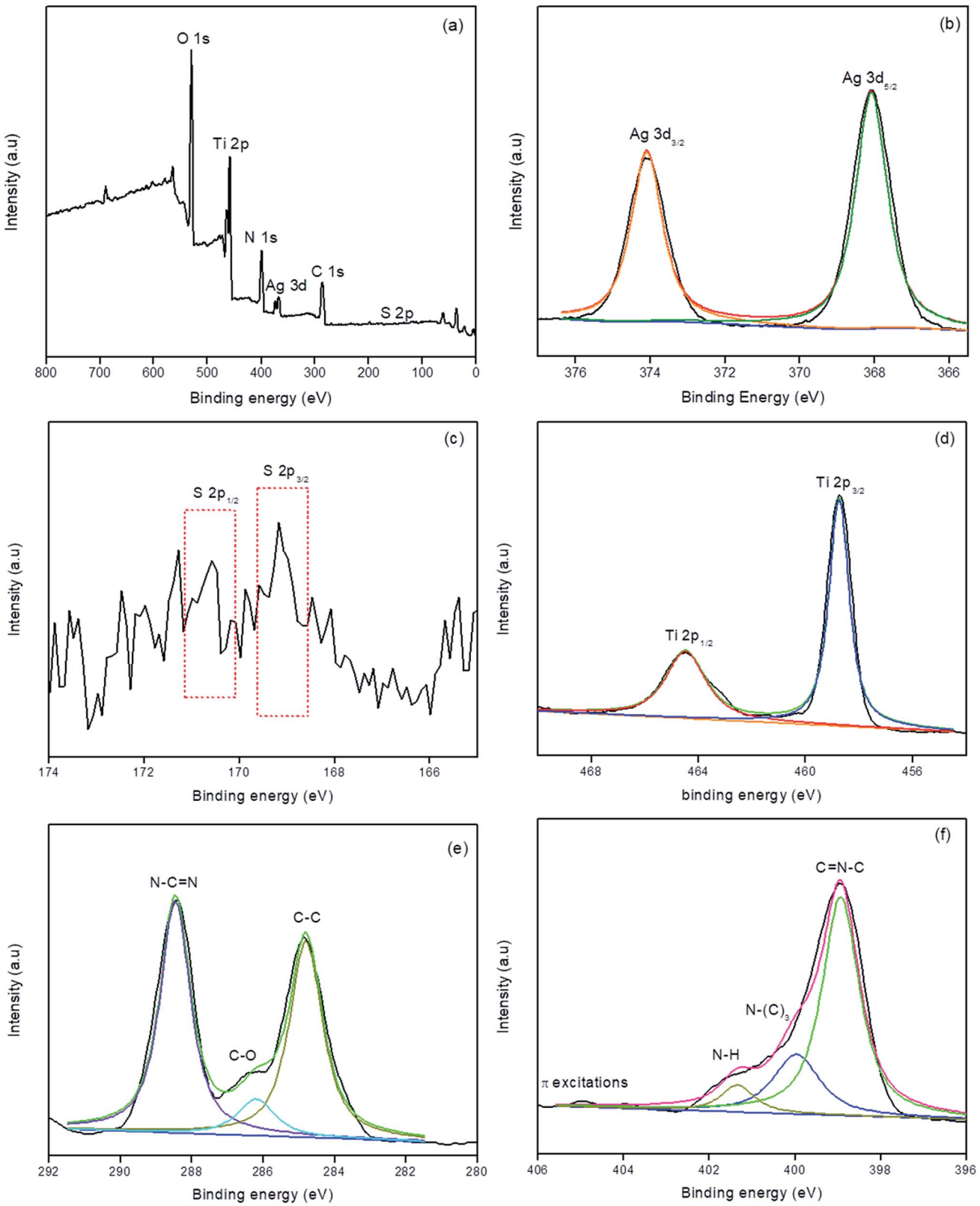


Fig. 3 XPS survey spectrum (a), high-resolution Ag 3d (b), S 2p (c), Ti 2p (d), N 1s (e), and C 1s (f) spectra of S/Ag–$TiO_2$@g-$C_3N_4$.

a Central Composite Design. The RSM modeling led to the development of a quadratic polynomial model (Table 2) to ascertain the degradation percentage of TS. A second-order polynomial expression shown in eqn (1) consisting of 15 coefficients was attained from the analysis of variance (ANOVA) at 95% confidence level ($p < 0.05$).

Table 3 ANOVA results for quadratic model[a]

| Source | Sum of squares | Degree of freedom | Mean square | *F*-value | *p*-value |
|---|---|---|---|---|---|
| Model | 2803.40 | 14 | 200.24 | 33.54 | <0.0001 |
| $X_1$ | 3.64 | 1 | 3.64 | 0.6105 | 0.4547 |
| $X_2$ | 97.53 | 1 | 97.53 | 16.33 | 0.0029 |
| $X_3$ | 10.28 | 1 | 10.28 | 1.72 | 0.2220 |
| $X_4$ | 1.28 | 1 | 1.28 | 0.2144 | 0.6544 |
| $X_1X_2$ | 5.29 | 1 | 5.29 | 0.8860 | 0.3711 |
| $X_1X_3$ | 0.5625 | 1 | 0.5625 | 0.0942 | 0.7659 |
| $X_1X_4$ | 7.29 | 1 | 7.29 | 1.22 | 0.2978 |
| $X_2X_3$ | 1.56 | 1 | 1.56 | 0.2617 | 0.6213 |
| $X_2X_4$ | 4.84 | 1 | 4.84 | 0.8106 | 0.3914 |
| $X_3X_4$ | 2.40 | 1 | 2.40 | 0.4024 | 0.5417 |
| $X_1^2$ | 41.27 | 1 | 41.27 | 6.91 | 0.0274 |
| $X_2^2$ | 1118.53 | 1 | 1118.53 | 187.33 | <0.0001 |
| $X_3^2$ | 2.57 | 1 | 2.57 | 0.4302 | 0.5283 |
| $X_4^2$ | 13.27 | 1 | 13.27 | 2.22 | 0.1702 |
| Residual | 53.74 | 9 | 5.97 | | |
| Cor total | 2857.13 | 23 | | | |

[a] $R^2 = 0.9812$; adjusted $R^2 = 0.9519$; predicted $R^2 = 0.8683$.

$$Y\,(\%) = +90.49 + 0.4500X_1 - 2.33X_2 - 0.7556X_3 + 0.2667X_4 - 0.5750X_1X_2 + 0.1875X_1X_3 + 0.6750X_1X_4 + 0.3125X_2X_3 - 0.5500X_2X_4 + 0.3875X_3X_4 - 4.04X_1^2 - 21.04X_2^2 + 1.01X_3^2 - 2.29X_4^2 \quad (1)$$

where $Y$ represents the degradation efficiency (%) and $X_1$, $X_2$, $X_3$ and $X_4$ indicated the uncoded values of TS concentration, pH, catalyst weight and time respectively.

The analysis of variance (ANOVA) results incurred for the present model (Table 3) suggested the quadratic model which is significant because of its high *F*-value (33.54) and very low *p*-value (<0.0001). Furthermore, it is also indicated that the lack-of fit was not significant relative to the pure error. The correlation coefficient-$R^2$ value (0.9812) was in reasonable agreement with the adjusted-$R^2$ value (0.9519) which confirmed the close relationship between the actual and predicted values of TS degradation percentage suggested by the model (Fig. 4a). Furthermore, the normal probability plot of the residuals showed that there is almost no violation of the assumptions: errors are normally distributed and independent, as the error variance is homogeneous (Fig. 4b). Moreover, the present model has an adequate precision due its signal to noise ratio value of 16.36, which is >4.[42] Accordingly, the model developed in the present study could be dependably used to navigate the design space. The *F*-values of variables suggested the order of independent parameters that influenced the TS degradation efficiency as follows: pH ($X_2$) > catalyst weight ($X_3$) > TS concentration ($X_1$) > reaction time ($X_4$).

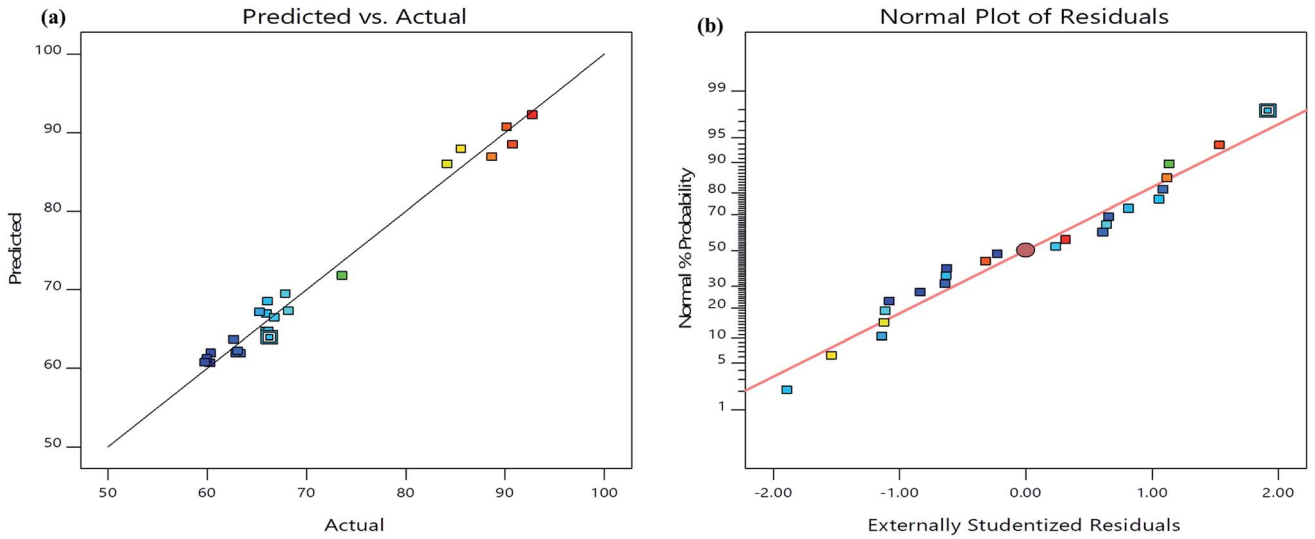


Fig. 4 (a) The relationship of predicted and actual values of the RSM model; (b) the internally studentized residuals *versus* normal % probability distribution.

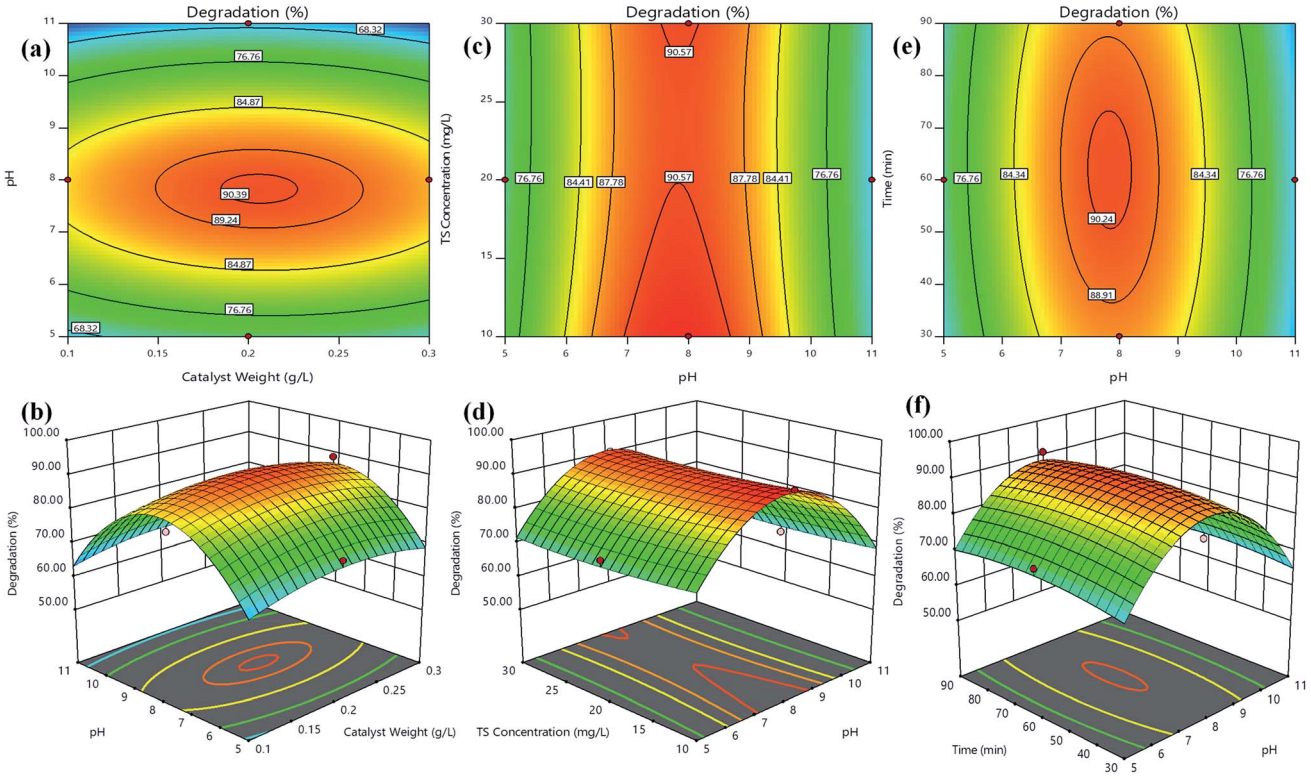


Fig. 5 Contours and 3D surface plots of TS degradation efficiency (%) for (a and b) catalyst weight *vs.* pH, (c and d) TS concentration *vs.* pH and (e and f) time *vs.* pH, respectively.

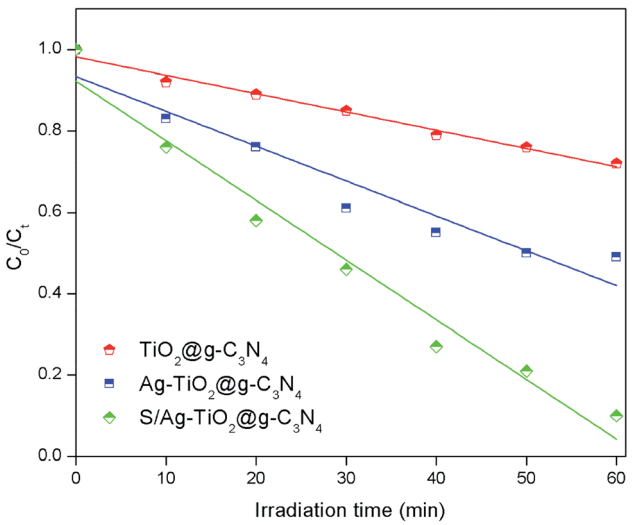


Fig. 6 TS degradation efficiency using the different prepared catalysts under the optimized conditions (catalyst weight = 0.20 g $L^{-1}$, pH = 7.8, and TS concentration = 10 mg $L^{-1}$).

The response surfaces could be visualized as contours or/and 3D plots to constitute the variations in the response with respect to two variables, by keeping the other variable fixed.[43] Fig. 5 shows the contours and 3D surface response plots for TS degradation efficiency (%) as a function of (a and b) catalyst weight *vs.* pH, (c and d) TS concentration *vs.* pH and (e and f) time *vs.* pH, respectively. The central coordinate points among the utmost contour levels in each of the showed figures indicate the corresponding parameters optimum value. Fig. 5(a and b) indicated that the TS degradation efficiency was gradually increased with the increase in pH from 5–8 regardless TS concentration at low or high level. The information about the surface properties and influence of solution pH on photocatalytic degradation by S/Ag–$TiO_2$@g-$C_3N_4$ nanocomposite has not been available in the literature; it is hard to understand the pH role on TS degradation by S/Ag–$TiO_2$@g-$C_3N_4$. The triclosan can be transformed to triclosan anion in the basic pH (pH > 8) since the p$K_a$ value of triclosan is between 7.6 and 8.1. Hence, the triclosan adsorption was less in basic and acidic pH due to the repulsive force works between triclosan and $TiO_2$ catalyst in pH higher than 8. Thus at pH 7.5 the maximum degradation was achieved. The reactant/substrate quantity adsorbed on the catalyst surface is an important parameter since only this amount imparts to photocatalytic process apart from the whole solution. This adsorption quantity depends on the initial concentration. The TS degradation efficiency was decreased while increasing in concentration further to its optimum value (Fig. 5c and d). This could be justified that when the concentration of TS increases, more number of TS molecules are adsorbed on catalyst surface, while less number of photons are accessible to reach the catalyst surface which further leads to lower amounts of active species generation, thus leading to lower degradation efficiency. Meanwhile, the TS degradation efficiency increased

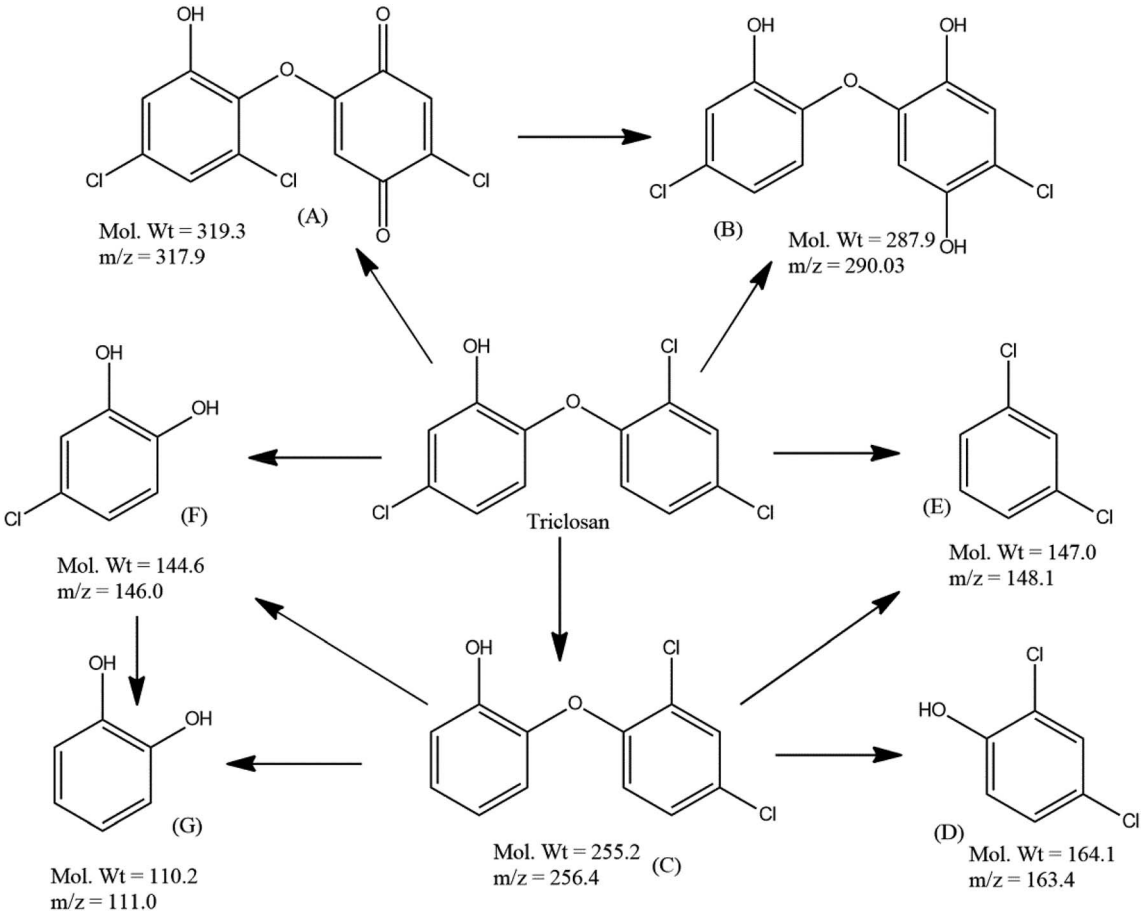


Fig. 7 Plausible degradation pathway of triclosan by S/Ag–$TiO_2$@g-$C_3N_4$ under the optimized conditions.

Table 4 Detoxification efficiency of the TS and its degradation products by using the prepared ternary composite, inoculum (*E. coli*) = 50 μL; TS concentration = 20 mg $L^{-1}$

| System | Irradiation time | CFU | Detoxification efficiency (%) |
|---|---|---|---|
| Control | — | 1326 | — |
| Untreated TS | — | 0 | 0 |
| Degradation products | 60 min | 852 ± 53 | 64.3 ± 3.9 |

with the increase in catalyst weight up to an optimum value (0.20 g $L^{-1}$) followed by decrease in the efficiency. The increase in catalyst weight higher to the optimum value could decrease the light penetration, by shielding effect and increases the agglomeration and sedimentation of nanoparticles which lead to decrease in the availability of active sites to the organic molecules.[44]

A verifying experiment was performed in order to check the optimum combination of the key operating parameters for degradation efficiency of TS under optimized conditions suggested by RSM model. Compared to the other prepared composites, the highest TS degradation efficiency (92.3%) was achieved under optimised conditions by S/Ag–$TiO_2$@g-$C_3N_4$ nanocomposite (Fig. 6 and S2†), indicating that the optimal conditions were practical. Thus, it could be concluded that the system to optimize the degradation conditions using RSM for the photocatalytic degradation of TS in this study was successful.

Furthermore, LC-ESI/MS analysis was performed in order to investigate the plausible degradation pathway of TS during visible light irradiation by S/Ag–$TiO_2$@g-$C_3N_4$ under the optimized conditions. LC-MS analysis of the TS degraded samples evidenced the presence of compounds with molecular weights 319.3, 287.9, 255.2, 164.1, 147.0, 144.6 and 110.2 which could be interpreted as (M+), (M+2), (M+), (M+), (M+), (M+), and (M+) peaks of structure A, B, C, D, E, F and G respectively (Fig. 7 and S3†).

### 3.3 Biotoxicity assessment

The toxicity tests could be based on animal, plant and bacterial bioassays. In general the bacterial bioassay methods includes bioluminescence and metabolic (*i.e.* population growth, respiration) inhibition assay. The various species includes *Vibrio fischeri*/*Photobacterium phosphoreum*, *Vibrio harveyi* and *Pseudomonas fluorescens* were used for bioluminescence inhibition assay, while *E. coli* and *Pseudomonas putida* were used for metabolic inhibition assay. Many researchers chosen *E. coli*

 

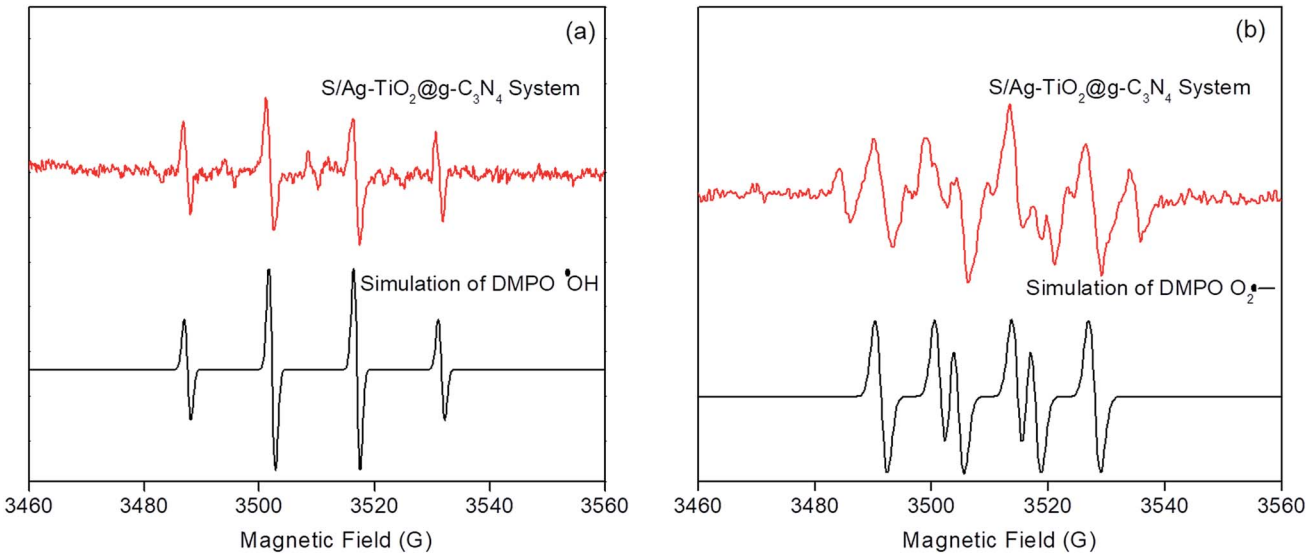


Fig. 8 ESR signals of ·OH (a) and $O_2^{\bullet -}$ (b) at ambient temperature.

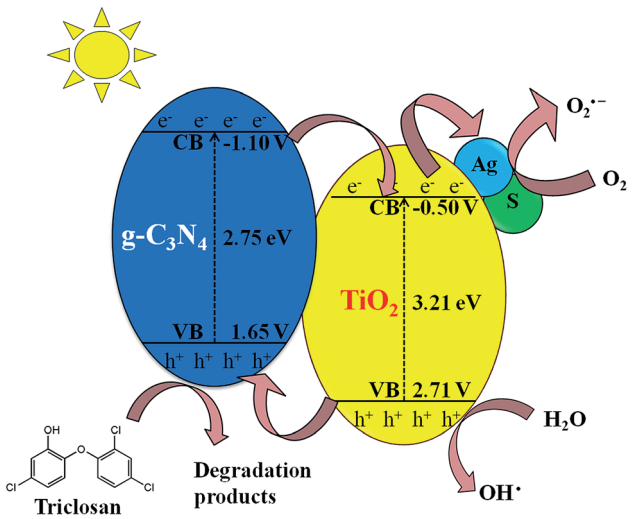


Fig. 9 Photocatalytic degradation mechanism of S/Ag–$TiO_2$@g-$C_3N_4$ nanocomposite under visible light.

strains because of their ability to easily respond with high sensitivity to different toxic compounds.[45,46]

In our study, according to rate of *E. coli* growth the pure TS showed 100% toxicity towards the bacteria due to its strong antibacterial activity. After 60 min of visible light irradiation, the mineralization products of TS showed 64.3 ± 3.9% (average data) of detoxification efficiency (Table 4 and S4†). Our study was according to the rate of *E. coli* growth (metabolic inhibition) in which the colony forming unit (CFU) assay measures the ability of *E. coli* to multiply. Thus, it represents and evaluates the reproductive power or condition of bacterial cells under normal physiological conditions or being exposed to other chemical compounds. The toxic products interfere with bacterial metabolism that involved in DNA replication, cell division and growth. Thus, the study gives a reliable measure of biotoxicity to the test chemicals. Our results indicated that during visible light irradiation the toxicity and antibacterial activity of the pure TS has been dramatically reduced to provide safety release of the solution into the water bodies in order to safe guard the several organisms in the ecosystem.

### 3.4 Photocatalytic degradation mechanism

The ESR technique was utilized to investigate the photocatalytic reaction mechanism and to analyze the active species participated in photodegradation of TS and over S/Ag–$TiO_2$@g-$C_3N_4$ under visible light. The signals corresponded to DMPO–·OH and DMPO–$O_2^{\bullet -}$ species could be substantiated from the standard spectra of ·OH ($A^N$ = 14.1 G and $A^H$ = 14.3 G; $g$ = 2.0132) and $\cdot O_2^-$ ($A^N$ = 13.3 G and $A^H$ = 11.3 G; $g$ = 2.0132) which was simulated by Bruker WinEPR SimFonia programme (Fig. 8a and b).[47–49] From the results it confirmed that ·OH, $O_2^{\bullet -}$ and photogenerated holes were the major species involved in photocatalytic process.

Based on the ESR results, the enhanced photocatalytic degradation mechanism of S/Ag–$TiO_2$@g-$C_3N_4$ under visible light was explained by Fig. 9. The CB and VB potentials of $TiO_2$ are around −0.50 and 2.71 eV,[50,51] while potentials of g-$C_3N_4$ are around −1.11 and 1.65 eV respectively.[52,53] The CB potential of g-$C_3N_4$ (−1.12 eV) is more negative than $TiO_2$ (−0.5 eV), hence the photogenerated electrons initially transferred from VB of g-$C_3N_4$ to CB, later could easily transfer from CB of g-$C_3N_4$ to CB of $TiO_2$. Meanwhile, $TiO_2$ absorb the UV light and transfer the electrons to CB from its VB. The Ag Fermi levels are lower than the CB of $TiO_2$.[54] Thus, the electrons on the $TiO_2$ CB could further transfer to the surface of silver nanoparticles. Furthermore, the doped sulfur leads to the formation of mid-gap energy levels such as S 2p between the valence band of O 2p and conduction band of Ti 3d.[55] This further reduces the $TiO_2$ band gap. The enhanced visible light activity is attributed to the formation

of hetero-junction electric field among the g-$C_3N_4$/$TiO_2$. The transfers of electrons from g-$C_3N_4$ CB to $TiO_2$ CB and further from CB of $TiO_2$ to silver was greatly suppressed the recombination of electron–hole pairs. These photogenerated electrons further react with adsorbed $O_2$ on the catalyst surface to form $O_2^{\bullet-}$ radicals which further combine with $H_2O$ to transforms to ·OH radicals. In the meantime, the holes in g-$C_3N_4$ VB was less positive than ·OH/$H_2O$ redox potential (2.68 eV *vs.* SHE),[56] indicating that the holes on g-$C_3N_4$ may not able to oxidize $H_2O$ into ·OH radicals, while they directly participate in the degradation. Meanwhile, holes on $TiO_2$ VB are more positive than ·OH/$H_2O$ redox potential which could react with $H_2O$ to generate highly reactive ·OH radicals. These $O_2^{\bullet-}$, ·OH, $h^+$ and $e^-$ species are highly reactive towards TS degradation to generate the degradation products, resulting in the efficient photocatalytic activity over S/Ag–$TiO_2$@g-$C_3N_4$ composite under visible light.

## 4. Conclusions

The present study deals with preparation of S and Ag doped $TiO_2$@g-$C_3N_4$ hybrid catalyst for efficient detoxification of triclosan. The results suggested that the doped Ag, S atoms and hetero-junction formation between $TiO_2$ and g-$C_3N_4$ could remarkably enhance the visible light activity. RSM modeling and optimization of the process illustrated that catalyst weight and pH are the most influential factors in photocatalytic degradation of TS. Around 92.3% of degradation was achieved under the optimized conditions after 60 min by the prepared photocatalyst. The plausible degradation pathway was proposed based on LC-ESI/MS results and the biotoxicity test suggested that less toxic degradation products were generated during the degradation. The strong interfacial contact present in S/Ag–$TiO_2$@g-$C_3N_4$ composite was highly retarded the charge recombination. Thus, S/Ag–$TiO_2$@g-$C_3N_4$ composites could be possible photocatalyst prospect applied for degradation and detoxification of various environmental pollutants.

## Conflicts of interest

There are no conflicts to declare.

## Acknowledgements

This study was financially supported by the Major Science and Technology Program for Water Pollution Control and Treatment (2018ZX07208010-01), Six Talent Peaks Project in Jiangsu Province, and 333 Talent Project Foundation of Jiangsu Province.

## References

1 B. Chen, Y. Yang, X. Liang, K. Yu, T. Zhang and X. Li, *Environ. Sci. Technol.*, 2013, **47**, 12753–12760.
2 Y. Luo, D. Mao, M. Rysz, Q. Zhou, H. Zhang, L. Xu and P. J. J. Alvarez, *Environ. Sci. Technol.*, 2010, **44**, 7220–7225.
3 L. Rizzo, C. Manaia, C. Merlin, T. Schwartz, C. Dagot, M. C. Ploy, I. Michael and D. Fatta-Kassinos, *Sci. Total Environ.*, 2013, **447**, 345–360.
4 A. B. A. Boxall, M. A. Rudd, B. W. Brooks, V. L. Trudeau and G. Van Der Kraak, *Environ. Health Perspect.*, 2012, **120**, 1221–1229.
5 Y. Gao, Y. Ji, G. Li and T. An, *Water Res.*, 2014, **49**, 360–370.
6 J. Wang and S. Wang, *J. Environ. Manage.*, 2016, **182**, 620–640.
7 X. Qiao, X. Zheng, Q. Xie, X. Yang, J. Xiao, W. Xue and J. Chen, *J. Hazard. Mater.*, 2014, **275**, 210–214.
8 J. M. Poyatos, M. Muñio, M. Almecija, J. Torres, E. Hontoria and F. Osorio, *Water, Air, Soil Pollut.*, 2010, **205**, 187–204.
9 M. Sun, Y. Wang, Y. Fang, S. Sun and Z. Yu, *J. Alloys Compd.*, 2016, **684**, 335–341.
10 Y. Yao, M. Sun, Z. Zhang, X. Lin, B. Gao, S. Anandan and W. Liu, *Int. J. Hydrogen Energy*, 2019, **44**, 9348–9358.
11 R. Asahi, T. Morikawa, T. Ohwaki, K. Aoki and Y. Taga, *Science*, 2001, **293**, 269–271.
12 Y. Yao, M. Sun, X. Yuan, Y. Zhu, X. Lin and S. Anandan, *Ultrason. Sonochem.*, 2018, **49**, 69–78.
13 M. Sun, Y. Kong, Y. Fang, S. Sood, Y. Yao, J. Shi and A. Umar, *Dalton Trans.*, 2017, **46**, 15727–15735.
14 X. Lin, M. Sun, Y. Yao and X. Yuan, *Electrochim. Acta*, 2018, **291**, 319–327.
15 R. Dholam, N. Patel, M. Adami and A. Miotello, *Int. J. Hydrogen Energy*, 2009, **34**, 5337–5346.
16 S. Zhou, Y. Liu, J. Li, Y. Wang, G. Jiang, Z. Zhao, D. Wang, A. Duan, J. Liu and Y. Wei, *Appl. Catal., B*, 2014, **158–159**, 20–29.
17 X. Wang, K. Maeda, A. Thomas, K. Takanabe, G. Xin, J. M. Carlsson, K. Domen and M. Antonietti, *Nat. Mater.*, 2009, **8**, 76–80.
18 S. Yin, J. Han, T. Zhou and R. Xu, *Catal. Sci. Technol.*, 2015, **5**, 5048–5061.
19 J. X. Wang, J. Huang, H. L. Xie and A. L. Qu, *Int. J. Hydrogen Energy*, 2014, **39**, 6354–6363.
20 Y. Chen, W. Huang, D. He, Y. Situ and H. Huang, *ACS Appl. Mater. Interfaces*, 2014, **6**, 14405–14414.
21 K. Sridharan, E. Jang and T. J. Park, *Appl. Catal., B*, 2013, **142**, 718–728.
22 A. G. Khosroshahi and A. Mehrizad, *J. Mol. Liq.*, 2019, **275**, 629–637.
23 M. Vaez, A. Z. Moghaddam and S. Alijani, *Ind. Eng. Chem. Res.*, 2012, **51**, 4199–4207.
24 I. Yahiaoui, F. Aissani-Benissad, K. Madi, N. Benmehdi, F. Fourcade and A. Amrane, *Ind. Eng. Chem. Res.*, 2013, **52**, 14743–14751.
25 Y. Wang, X. C. Wang and M. Antonietti, *Angew. Chem., Int. Ed.*, 2012, **51**, 68–89.
26 W. J. Ong, L. L. Tan, S. P. Chai and S. T. Yong, *Dalton Trans.*, 2015, **44**, 1249–1257.
27 S. Naraginti, Y. Li, Y. Wu, C. Zhang and A. R. Upreti, *RSC Adv.*, 2016, **6**, 87246–87257.
28 E. Anodization, J. Wang and Z. Lin, *Chem. Mater.*, 2008, **20**, 1257–1261.

 

29 K. Kočí, M. Reli, I. Troppová, M. Šihor, J. Kupková, P. Kustrowski and P. Praus, *Appl. Surf. Sci.*, 2017, **396**, 1685–1695.
30 A. Raza, H. Shen, A. A. Haidry and S. Cui, *Appl. Surf. Sci.*, 2019, **488**, 887–895.
31 T. S. Wu, K. X. Wang, G. D. Li, S. Y. Sun, J. Sun and J. S. Chen, *ACS Appl. Mater. Interfaces*, 2010, **2**, 544–550.
32 P. Christopher, D. B. Ingram and S. Linic, *J. Phys. Chem. C*, 2010, **114**, 9173–9177.
33 M. Zang, L. Shi, L. Liang, D. Li and J. Sun, *RSC Adv.*, 2015, **5**, 56136–56144.
34 S. Naraginti, Y. Li and Y. Wu, *RSC Adv.*, 2016, **6**, 75724–75735.
35 Y. Lai, H. Zhang, K. Xie, D. Gong, Y. Tang, L. Sun, C. Lin and Z. Chen, *New J. Chem.*, 2010, **34**, 1335–1340.
36 C. McManamon, J. O'Connell, P. Delaney, S. Rasappa, J. D. Holmes and M. A. Morris, *J. Mol. Catal. A: Chem.*, 2015, **406**, 51–57.
37 S. Abu and C. Ribeiro, *J. Mol. Catal. A: Chem.*, 2016, **412**, 78–92.
38 K. V. Bineesh, S. Y. Kim, B. R. Jermy and D. W. Park, *J. Ind. Eng. Chem.*, 2009, **15**, 207–211.
39 Y. Kim, J. Lee, H. Jeong, Y. Lee, M. H. Um, K. M. Jeong, M. K. Yeo and M. Kang, *J. Ind. Eng. Chem.*, 2008, **14**, 396–400.
40 J. Mao, T. Peng, X. Zhang, K. Li, L. Ye and L. Zan, *Catal. Sci. Technol.*, 2013, **3**, 1253–1260.
41 S. Zhang, J. Li, X. Wang, Y. Huang, M. Zeng and J. Xu, *ACS Appl. Mater. Interfaces*, 2014, **6**, 22116–22125.
42 M. A. Bezerra, R. E. Santelli, E. P. Oliveira, L. S. Villar and L. A. Escaleira, *Talanta*, 2008, **76**, 965–977.
43 C. L. Ai, D. D. Zhou, Q. Wang, X. W. Shao and Y. J. Lei, *Sol. Energy*, 2015, **113**, 34–42.
44 B. Neppolian, H. Choi, S. Sakthivel, B. Arabindoo and V. Murugesan, *J. Hazard. Mater.*, 2002, **89**, 303–317.
45 S. Belkin, D. R. Smulski, A. C. Vollmer, T. K. Van Dyk and R. A. LaRossa, *Appl. Environ. Microbiol.*, 1996, **62**, 2252–2256.
46 S. Belkin, D. R. Smulski, S. Dadon, A. C. Vollmer, T. K. Van Dyk and R. A. LaRossa, *Water Res.*, 1997, **31**, 3009–3016.
47 B. Jiang, X. Wang, Y. Liu, Z. Wang, J. Zheng and M. Wu, *J. Hazard. Mater.*, 2016, **304**, 457–466.
48 D. R. Duling, *J. Magn. Reson., Ser. B*, 1994, **104**, 105–110.
49 J. Zou, J. Ma, L. Chen, X. Li, Y. Guan, P. Xie and C. Pan, *Environ. Sci. Technol.*, 2013, **47**, 11685–11691.
50 C. Zhao, A. Krall, H. Zhao, Q. Zhang and Y. Li, *Int. J. Hydrogen Energy*, 2012, **37**, 9967–9976.
51 Y. Bessekhouad, D. Robert and J. V. Weber, *J. Photochem. Photobiol., A*, 2004, **163**, 569–580.
52 X. Wang, K. Maeda, A. Thomas, K. Takanabe, G. Xin, J. M. Carlsson, K. Domen and M. Antonietti, *Nat. Mater.*, 2009, **8**, 76–80.
53 S. C. Yan, S. B. Lv, Z. S. Li and Z. G. Zou, *Dalton Trans.*, 2010, **39**, 1488–1491.
54 K. Koci, K. Mateju, L. Obalova, S. Krejcikova, Z. Lacny, D. Placha, L. Capek, A. Hospodkova and O. Solcova, *Appl. Catal., B*, 2010, **96**, 239–244.
55 T. Umebayashi, T. Yamaki, S. Tanala and K. Asai, *Chem. Lett.*, 2003, **1**, 330–331.
56 S. Zhao, S. Chen, H. Yu and X. Quan, *Sep. Purif. Technol.*, 2012, **99**, 50–54.